*International Journal of Remote Sensing*
Vol. 27, No. 9, 10 May 2006, 1839–1853

Taylor & Francis
Taylor & Francis Group

# Stereo cloud-top height retrieval with ASTER and MISR

GABRIELA SEIZ*†, ROGER DAVIES‡ and ARMIN GRÜN†
†Institute of Geodesy and Photogrammetry, Swiss Federal Institute of Technology ETH, ETH-Hönggerberg, 8093 Zürich, Switzerland
‡Jet Propulsion Laboratory, California Institute of Technology, 4800 Oak Grove Drive, Pasadena, CA 91109, USA

(*Received 31 March 2005; in final form 15 September 2005*)

The combined multi-view photogrammetric retrieval of cloud-top height (CTH) from the Advanced Spaceborne Thermal Emission and Reflection Radiometer (ASTER) and the Multi-angle Imaging SpectroRadiometer (MISR) is discussed. Although ASTER was designed mainly for land applications, the synergistic use of MISR and ASTER is shown to be valuable for 3D cloud analysis. A new cloud-adapted matching algorithm based on least-squares matching (LSM) was used for the photogrammetric processing of both MISR and ASTER. The methods were applied to an ASTER scene over Zürich-Kloten, Switzerland, in April 2002, which was acquired on-demand. This case study, with coincident ASTER, MISR and Meteosat-6 10-minute Rapid Scans, is treated in detail. As a matching validation option it is shown that, by chance, the cloud motion error for the MISR An-Aa and ASTER stereo CTHs is approximately the same, independent of the actual cloud height and cloud motion. It was therefore possible to evaluate the accuracy of the MISR An-Aa matching versus the ASTER matching, independent of artefacts due to the subsequent wind correction. The results were also compared to the operational MISR L2TC stereo CTH results. The results obtained by each of these methods yield consistent values for CTH (uncorrected for wind motion).

## 1. Introduction

Stereoscopy of clouds has a long tradition in meteorology (Hasler 1981). From satellites, both geostationary and polar-orbiting sensors can be used, as described in Fujita (1982). Stereo measurements have the advantage that they depend only on basic geometric relationships of observations of cloud features from at least two different viewing angles, while other cloud-top height (CTH) estimation methods are dependent on the knowledge of additional atmospheric parameters such as cloud emissivity, ambient temperature or lapse rate.

The Multi-angle Imaging SpectroRadiometer (MISR) is currently the only operational multi-view sensor that acquires images from nine different viewing angles. The MISR team has pioneered spaceborne, near-simultaneous, multi-view imaging from a single satellite, thus providing a new, passive, optical technology for retrieving CTH and cloud-top wind (CTW) values simultaneously (Diner *et al.* 1999, Horváth and Davies, 2001, Moroney *et al.* 2002, Zong *et al.* 2002). The second instrument with stereo capability onboard Terra, the Advanced Spaceborne

*Corresponding author. Email: gabriela.seiz@esa.int

*International Journal of Remote Sensing*
ISSN 0143-1161 print/ISSN 1366-5901 online 
http://www.tandf.co.uk/journals
DOI: 10.1080/01431160500380703

Thermal Emission and Reflection Radiometer (ASTER), was designed mainly for land applications (Yamaguchi *et al.* 1998). Because of the high spatial resolution of the stereo channel of 15 m, ASTER is also useful for cloud studies. As ASTER only incorporates two view angles, cloud height and velocity cannot be uniquely separated as for MISR. With no further assumptions, the ASTER CTHs have to be corrected with cloud advection data from another source. However, with knowledge of further information on the actual situation, for example direction of motion of aerosol plumes, the height and advection speed can be retrieved, as described by Urai (2004).

In this paper we describe the stereo-photogrammetric methodology to derive CTH and CTW from ASTER and MISR, and how the two instruments complement each other for this retrieval. A case study over Zürich-Kloten, Switzerland, with on-demand ASTER data acquisition, is presented and the MISR and ASTER CTH results compared.

## 2. Data

The two sensors ASTER and MISR onboard the NASA EOS-Terra spacecraft, launched in December 1999, were used in this study. The Terra orbit is sun-synchronous at a mean height of 705 km, with an inclination of 98.5° and an equatorial crossing time of about 10:30 local solar time. The repeat cycle is 16 days. In the following two sections, the data characteristics for ASTER and MISR, shown in table 1, are explained further.

### 2.1 *ASTER*

The ASTER is an advanced multispectral imager that covers a wide spectral region with 14 bands from the visible to the thermal infrared with high spatial, spectral and radiometric resolution (Yamaguchi *et al.* 1998). The sensor consists of three separate instrument subsystems, the Visible and Near Infrared (VNIR), the Shortwave Infrared (SWIR) and the Thermal Infrared (TIR). The VNIR subsystem has three bands (named 1, 2 and 3N) and an additional backward telescope for stereo (named 3B). The configuration of the ASTER stereo channel, channel 3, is illustrated in figure 1 (Lang and Welch 1999).

The available ASTER data products are described in Abrams (2000). The ASTER Level 1B data used are L1A data with radiometric and geometric coefficients applied. The L1B image is projected into the Universal Transverse Mercator (UTM)

Table 1. Characteristics of the multi-view satellite sensors used in this study. For ASTER, only the characteristics of the stereo band 3N/3B are listed.

| | ASTER | MISR |
|---|---|---|
| System type | Linear CCD array | Linear CCD array |
| Data acquisition | On-demand | Continuous |
| Viewing angles (°) | 0.0, –27.6 | 0.0, ±26.1, ±45.6, ±60.0, ±70.5 |
| Time delay between consecutive views (s) | 55 | 45–60 |
| Spatial resolution (m) | 15 | 275 |
| Spectral channels (μm) | 0.82 | 0.45, 0.55, 0.67, 0.87 |
| Radiometric resolution | 8-bit | 14-bit |

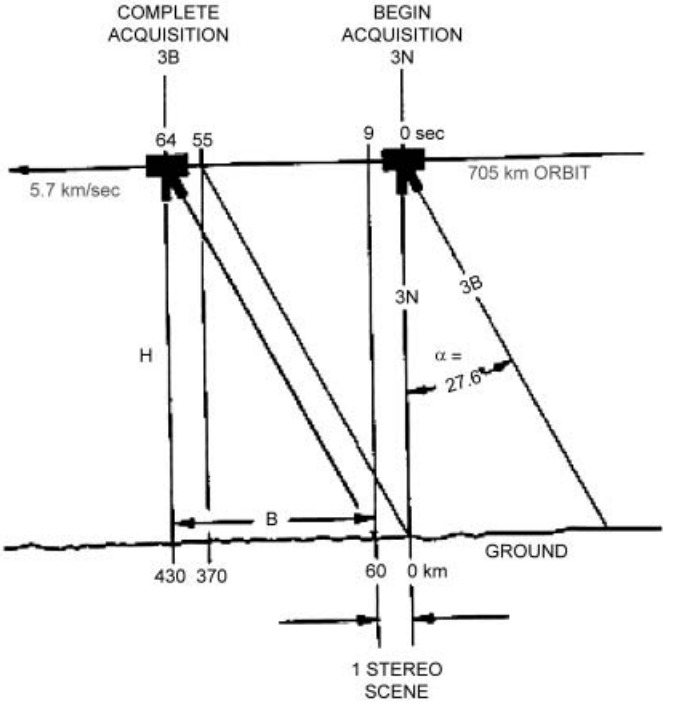


Figure 1. ASTER stereo configuration.

(default) or Space Oblique Mercator (SOM) projection, covering an area of about 60 km × 60 km, with a grid spacing of approximately the full instrument resolution.

In contrast to all other sensors on EOS-Terra (i.e. MISR, MODIS, CERES), ASTER does not acquire data continuously because of the huge amount of data it generates, but only on specific dates/orbits (i.e. on demand). For cloud studies in coincidence with our ground-based imager system it was necessary to order an ASTER image acquisition, as the probability of an automatic ASTER image being coincident with our ground-based system was practically zero, as the ASTER field of view only includes Zürich-Kloten airport twice (paths 194 and 195) within the 16-day repeat cycle. On-demand scheduling of satellite image acquisition is a challenging exercise. There are many parameters that can prevent a successful delivery of a scene, such as conflicting demands with different priorities, wrong scheduling, and transmission failures. For ASTER, the on-demand orders had to be submitted at least 2 months in advance of the field campaign. From a total of eight dates within three separate campaigns during September 2001, November 2001 and April 2002, only one acquisition on 12 April 2002 succeeded with coincident ground-based measurements. The other seven dates failed due to 'no clouds', 'rain', 'cancelled' or 'failed' image acquisition.

Geolocation accuracy of the ASTER L1B nadir and backward scenes was checked with 20 ground control points (GCPs) around the 'Zugersee', 'Baldeggersee' and 'Halwylersee'. The GCPs were measured manually in the Swiss national map 1 : 25 000 with an accuracy of about 10 m in X and Y and a height accuracy of 5 m. Using the 20 GCPs, the mean difference and standard deviation between the GCP coordinates and the ASTER pixel coordinates, as interpolated from the header file,

were –3.5 m and 22.4 m in the X direction and –0.7 and 27.2 m in the Y direction. Consequently, there was no significant systematic error in the ASTER georeferencing and the ASTER images were geolocated with an accuracy of better than 2 pixels, or 30 m. Thus, with the ASTER data simultaneous to MISR, we have a reference dataset for CTH retrieval with about 5 times better accuracy than MISR (i.e. 30 m versus 140 m). Similar points between MISR and ASTER can be found by matching of the fourth pyramid level of ASTER (resolution $2^4 \times 15\,\text{m} = 240\,\text{m}$) and the original level of MISR (resolution 275 m) (figure 2).

### 2.2 *MISR*

The MISR instrument is currently the only operational satellite sensor to offer multi-view stereo images. It consists of nine pushbroom cameras at different viewing angles, –70.5°(named Da), –60.0° (Ca), –45.6° (Ba), –26.1° (Aa), 0.0° (An), 26.1° (Af), 45.6° (Bf), 60.0° (Cf), and 70.5° (Df), acquiring images in four spectral bands.

The operational data products from MISR are described in Lewicki *et al.* (1999). The two products used for this study are the L1B2 ellipsoid-projected radiance data product and the L2TC top-of-atmosphere/cloud product. The L1B2 ellipsoid-projected radiance product is referenced to the surface of the WGS84 ellipsoid with

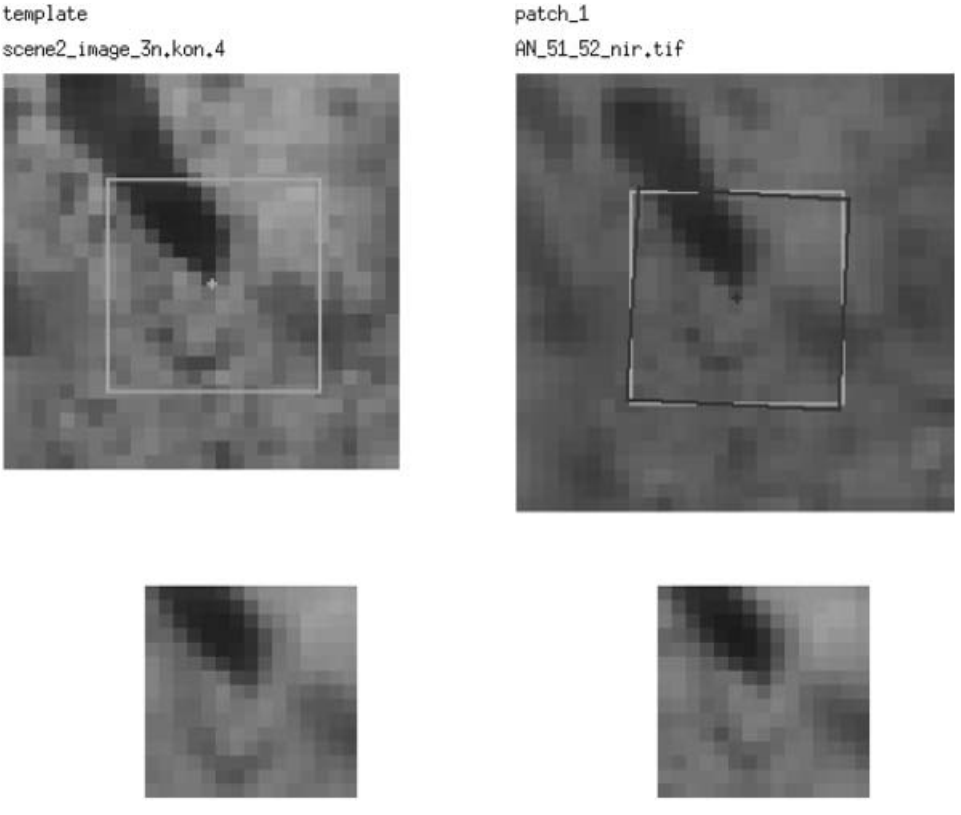


Figure 2. Measurement of similar points in the ASTER fourth pyramid level (left) and MISR original level (right) images.

no terrain elevation included. The SOM projection (Snyder 1987) was selected as the reference map grid because it is specifically suited for continuous mapping of satellite imagery. The MISR georectified product spatial horizontal accuracy requirements are driven by the needs of the geophysical parameter retrieval algorithms. The goal of operational MISR data processing is to achieve an uncertainty better than $\pm 140$ m for both the absolute geolocation of the nadir camera and the co-registration between all nine cameras (Jovanovic *et al.* 2002). The detailed theory on the georectification algorithms and the in-flight camera geometric model (CGM) calibration is described in Jovanovic *et al.* (1999a,b). The latest evaluation results for CGM versions 6 and 7 shown in Jovanovic *et al.* (2002) are approaching prelaunch requirements, with along- and cross-track errors far below 1 pixel for all cameras, except the Da camera.

As the MISR red channel is, in general, the only spectral channel with full resolution in all nine views, multi-spectral matching differences within multi-layer clouds, as for example the Along-Track Scanning Radiometer (ATSR2) onboard ERS-2, cannot be generated with MISR. However, matching tests with ATSR2 showed that the main differences in the CTH results occur between the visible and the thermal infrared channels, while the differences between visible/near-infrared channels or between infrared channels are small (Seiz 2003).

The L1B2 ellipsoid-referenced data product was used for the CTH and CTW calculations presented in this study. For identification of the exact acquisition time of each pixel, the L1B2 SOM grid location has to be back-projected to the original line/pixel position within the MISR swath, and this can be achieved with the transformation parameters stored in the L1B2 ancillary data. The exact view zenith angles for each camera, which are also needed for the CTH calculation, are available in the geometric parameters (GPs) product, which supplies the sun and view zenith angles on the WGS84 ellipsoid relative to a normal to that surface, as well as azimuth angles relative to local North. These angles are reported with a grid spacing of 17.6 km. The view zenith and azimuth angles are based upon the reported spacecraft attitude and position and the calibrated camera model.

The L2TC product contains the operationally derived cloud parameters, such as stereo CTH, east–west (EW) and north–south (NS) cloud motion components, as well as many additional parameters from the stereo retrieval. The operational matching algorithms and strategies of the MISR team for the L2TC CTH/CTW retrieval are fully described in Diner *et al.* (1999) and Muller *et al.* (2002). In brief, they are a tuned compromise of accuracy, coverage and computational efficiency. The winds are retrieved using a sparse feature matcher called NestedMax that uses inequality logic to find sets of local brightness maxima in 1D strings of radiances within a given mesoscale domain. Each set is analysed similarly up to five times, producing nested sets, up to the brightest radiance in the domain. The sets are then compared for uniqueness to obtain a sparse set of matches between the two images of a given pair. More complete coverage is then obtained by the M2 and M3 matchers, which are area matchers that seek a minimum difference in brightness patterns between small image patches that are moved with respect to each other. The differences are calculated at the pixel level (i.e. no sub-pixel enhancement is attempted due to operational constraints) with a minimum of floating point operations. The M2 matcher is faster but with poorer coverage than M3, so the latter is used when M2 fails. The joint matcher is termed M23.

## 3. Stereo CTH retrieval

Determination of CTH from ASTER or any two views of MISR proceeds along the same cloud-adapted processing scheme (figure 3). First, all images were reduced to 8-bit with linear stretching between the minimum and maximum values. As no a priori values of the cloud heights were given to the matching algorithm, the number of pyramid levels for the hierarchical matching was chosen so that the maximum possible parallax at the highest level was only 1–2 pixels. Four and seven pyramid levels were used for MISR and ASTER, respectively. The images on every pyramid level were enhanced and radiometrically equalized with a Wallis filter (Wallis 1976, Baltsavias 1991), which is an adaptive, local filter, defined with the objective of forcing the mean and standard deviation of an image to given target values. The filtered image is calculated as

$$\text{img\_new}(x,y) = \text{img}(x,y)\, r_1 + r_0 \tag{1}$$

where

$$r_1 = c\frac{s_f}{cs_g + (1-c)s_f}$$

$$r_0 = bm_f + (1-b-r_1)m_g$$

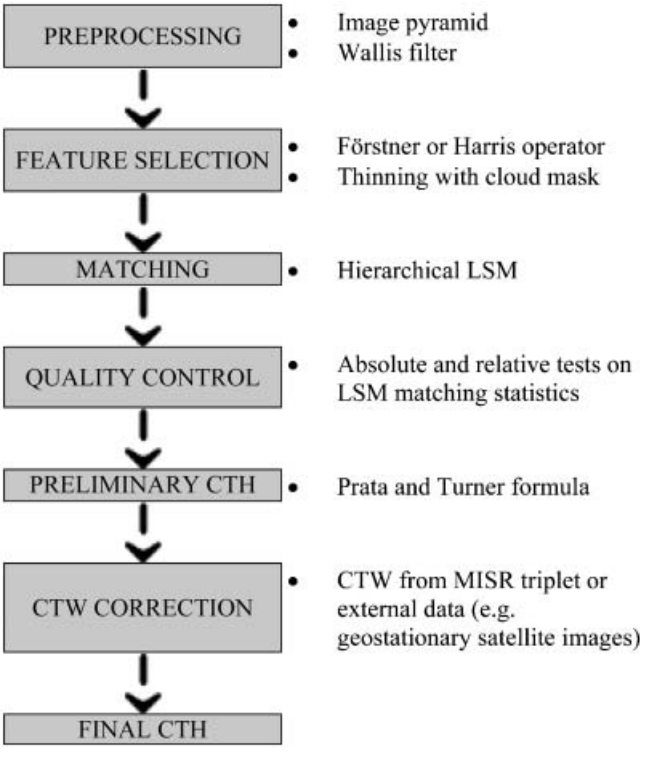


Figure 3. Schematic overview of stereo-photogrammetric processing of the satellite-based images to derive cloud-top height (CTH) and cloud-top wind (CTW).

($m_g$, $s_g$) are the original mean and standard deviation of each block, ($m_f$, $s_f$) are the target mean and standard deviation for every block, $b$ ($0 \leqslant b \leqslant 1$) is the brightness forcing constant and $c$ ($0 \leqslant c \leqslant 1$) is the contrast expansion constant. In areas with the same grey values (e.g. saturated areas) the filter cannot create any texture, but in areas with weak texture patterns the filtering strongly enhances the texture so that the images are optimized for matching. According to the block or filter size, different cloud structures can be enhanced. In general, a block size of about 70 pixels was chosen at the original level, which was then decreased up the pyramid.

Points with good texture were selected with the Förstner (Förstner and Gülch 1987) or Harris (Harris and Stephens 1988) interest operator. Both interest operators have been extensively used in photogrammetry and computer vision. In general, a corner or centre point is selected if its window grey-level signal ellipse is small and circular based on two thresholds, while an edge point is detected if its signal ellipse is extended in the edge direction. Points within textureless areas have large, approximately circular signal ellipses and are not extracted. The differences between the operators are the method to derive the grey-level signal ellipses and the applied thresholds. A comparison of the performance of various interest operators, including the Förstner and Harris operators, for different objects is described in Schmid *et al.* (1998).

The unconstrained Multi-Photo Geometrically Constrained (MPGC) least-squares matching (LSM) (Grün 1985, Baltsavias 1991) was applied hierarchically, starting on the highest pyramid level. The MPGC LSM solution is obtained by minimizing the squared sum of the grey value differences between template and patch image, including up to six parameters (i.e. affine transformation) to describe distortions of the patch image in relation to the template image. After each pyramid level, quality control with absolute tests on the LSM statistics was performed to exclude the largest blunders from further processing down the pyramid, as described below. The patch size was slightly increased from one pyramid level to the next, from $7 \times 7$ on the highest level to about $15 \times 15$ on the lowest level. The matching solutions on the lowest level were quality controlled with both absolute and relative tests on the LSM statistics.

For quality control, the MPGC matching algorithm provides several statistical measures for each matched point that can be used to detect and exclude gross errors, including the cross-correlation coefficient, a posteriori variance of unit weight from the least-squares adjustment, size of shifts, number of iterations, etc. None of these measures can safely detect all blunders without excluding good points and a combination of these quality measures provides better diagnostics. More details about these measures and their use are given in Baltsavias (1991) and Baltsavias and Stallmann (1993). In this study, both absolute and relative tests have been used, as described above. In the absolute tests, if one of the quality criteria had a poor value for a point, the point was excluded. The thresholds for these poor values were chosen carefully, as the aim was to exclude only large blunders, which may distort the statistics. Subsequently, for the relative tests, the thresholds were derived from the statistics of all match points and were expressed as functions of the mean value and the standard deviation of each criterion; for example, the threshold for the cross-correlation coefficient was defined as the mean value minus $n$ times the standard deviation, with $n$ usually set equal to 3. In all cases, such blunder detection tests improve the results significantly, although some blunders always remain undetected and some correct match points are falsely rejected. The tests lead to a

rejection of a certain percentage of the match points, usually about 5% in the absolute tests and 15–20% in the relative tests, depending on the matching problems and the selection of the thresholds.

The resulting $y$-parallaxes were converted into CTH according to Prata and Turner (1997):

$$\mathrm{CTH} = \frac{\Delta y}{\tan(\theta_1) - \tan(\theta_0)} \tag{2}$$

where $\Delta y$ is the along-track parallax, as derived from matching, and $\theta_0$ and $\theta_1$ are the zenith angles of the two views used. The height values of the successfully matched points were finally interpolated by triangulation to the full resolution grid.

The accuracy of the retrieved CTHs is dependent on the geometric stereo configuration expressed as the base-to-height ratio B/H, on the matching accuracy $\Delta y_p$, on the accuracy of the georectification, including the exact values of the zenith angles, and on the along-track motion retrieval accuracy $\Delta v'$. In table 2, the B/H values and time differences for ASTER and MISR An-Aa are listed, together with an estimation of the height error $\Delta h$, given an along-track parallax error $\Delta y_p$ of 0.5 pixel from matching or an along-track motion error $\Delta v'$ of 3 m/s. These error estimates of $\Delta y_p$ of $\pm 0.5$ pixel from MPGC LSM on clouds and of $\Delta v'$ of $\pm 3$ m/s from CTW retrieval from geostationary images (i.e. Meteosat-6 Rapid Scans) are based on a number of case studies treated in Seiz (2003).

For all view combinations, the height error due to motion errors is very prominent. With only two views, or symmetric multiple views, which is usually the case, the along-track cloud motion has to be corrected with data from an independent source. One possible source of independent data is geostationary satellite cloud motion information. Another possibility, making use of the advantage of several instruments on the Terra platform, is to apply the cloud motion data derived from MISR triplets. The CTH correction $\Delta h_{\mathrm{CTW}}$ is then calculated as

$$\Delta h_{\mathrm{CTW}} = \frac{v' \times \Delta t}{(B/H)} \tag{3}$$

where $v'$ is the along-track CTW component, $\Delta t$ is the time difference between the two views and B/H is the base-to-height ratio of the camera combination, as listed in table 2. This typically adds a bias error to the absolute height retrieval of about 100 m for every 1 m/s uncertainty in the along-track CTW component. We found that MISR An-Af, or An-Aa, stereo CTH and ASTER stereo CTH have about the same motion errors, independent of the actual cloud height. This offers the

Table 2. Base-to-height ratios, time differences and theoretical cloud-top height accuracy components $\Delta h_{\mathrm{matching}}$ and $\Delta h_{\mathrm{CTW}}$ between image pairs of ASTER and MISR.

| Sensor | Pixel size (m) | B/H | $\Delta t$ (s) | $\Delta h_{\mathrm{matching}}$ (m) (for $\Delta y_p$=0.5 pixel) | $\Delta h_{\mathrm{CTW}}$ (m) (for $\Delta v'$=3 m/s) |
|---|---|---|---|---|---|
| ASTER | 15 | 0.60 | 55.0 | 13 | 275 |
| MISR AN_AA | 275 | 0.49 | 45.3 | 280 | 277 |

possibility for high-resolution ASTER cloud matching that can be used as a validation digital surface model (DSM) for the coarser resolution MISR matching results.

## 4. Results

All the above-described methods were applied to a dataset over Switzerland on 12 April 2002 (Terra orbit 12321) with coincident images of MISR and ASTER. For the same period, Meteosat-6 10-minute Rapid Scan data were also available for cloud motion analysis (Seiz *et al.* 2003). The cloud situation as seen by MISR and ASTER is presented in figure 4, while the exact acquisition periods of the three satellite systems are listed table 3.

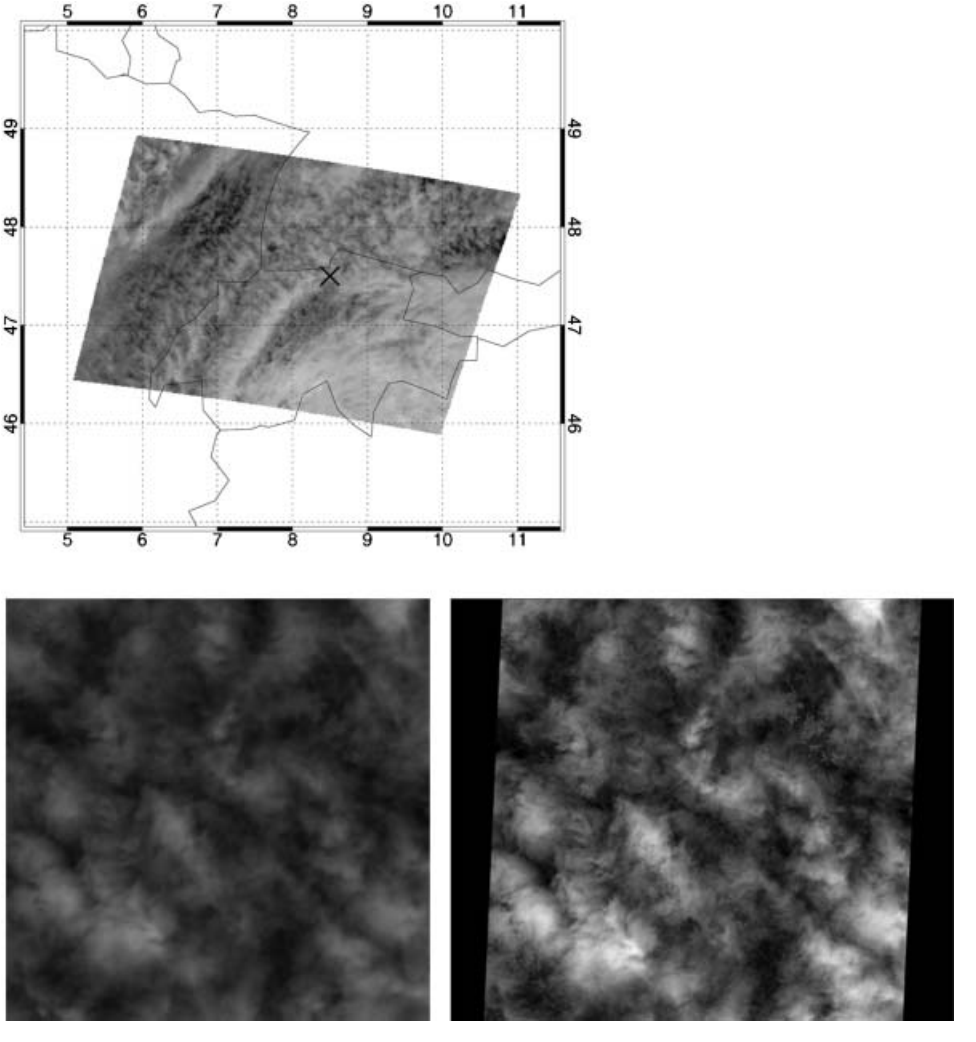


Figure 4. Cloud situation on 12 April 2002 over Zürich-Kloten, Switzerland. Top: MISR blocks 52-53 (black cross: Zürich-Kloten); bottom: MISR L1B2 data, zoom into part of block 52 (left) and ASTER L1B data (right). The area of the ASTER scene is approximately $60 \times 60$ km.

Table 3. Acquisition times (UTC) of MISR, ASTER and Meteosat-6 data over Zürich-Kloten, Switzerland, on 12 April 2002.

| Sensor | Acquisition time (at 47° N) | Frequency |
|---|---|---|
| MISR (block 52) | DF: 10:31:36, …, AN: 10:35:02, …, DA: 10:38:28 | 16 days |
| ASTER | 3N: 10:35:03, 3B: 10:35:58 | 16 days (on-demand only) |
| Meteosat-6 | 10:27:21/10:37:21/10:47:21/... | 10 min |

As shown in figure 5, corresponding cloud features can be found between the MISR and ASTER images by taking the fourth pyramid level of ASTER and the original level of MISR.

The extracted CTH fields, before any cloud motion correction, are shown in figure 6. The extracted height histograms from MISR L1B2 MPGC LSM, ASTER MPGC LSM and MISR L2TC M23 are shown in figure 7. Overall, there is good correspondence between all three extracted height fields. The ASTER histogram peaks at an uncorrected altitude of 11.0 km, and has a $1\sigma$ spread of 0.69 km, which is slightly broader than the 0.56 km spread of the MISR LSM histogram. This relative broadening of the natural variability in the CTH field may be introduced either by matching errors due to the higher resolution of the land areas that are visible between the clouds or by the difference of matching in the MISR red images against matching in the ASTER NIR channels. For the L2TC M23 results, the quantized CTHs due to the pixel-only accuracy of the M23 are readily apparent when plotted with a histogram bin size of 50 m. The peak of our MISR results for this case is centred at an uncorrected (for wind) altitude of 10.85 km, which is intermediate between the dominant two quantized peaks in the operational MISR L2TC results, at 10.70 km and 11.25 km. The peak at the higher altitude is more populated, consistent with the L2TC algorithm's approach of using the higher value of the matching retrievals from the An-Af and An-Aa camera pairs.

## 5. Conclusions

In this paper, we have outlined an interesting synergy between ASTER and MISR onboard EOS-Terra for cloud geometry analysis. Both multi-view sensors are able

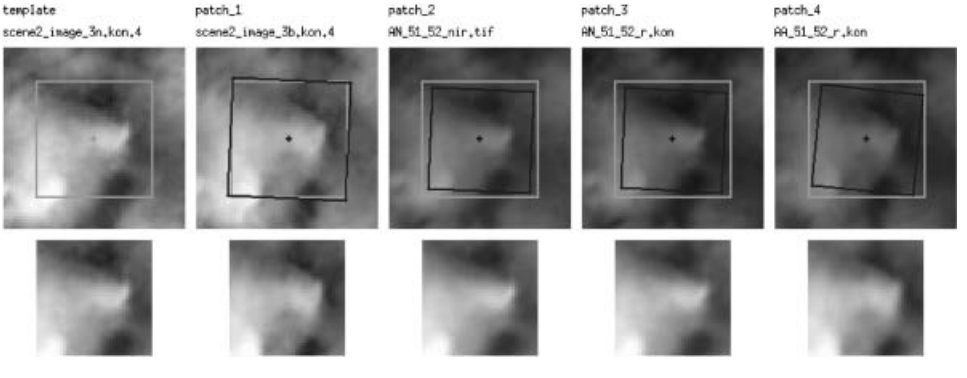


Figure 5. Cloud matching between ASTER (fourth pyramid level) and MISR (original level). Order of images (from left to right): ASTER nadir image (3N), ASTER backward image (3B), MISR nadir near-infrared image (AN_nir), MISR nadir red image (AN_r) and MISR backward red image (AA_r).

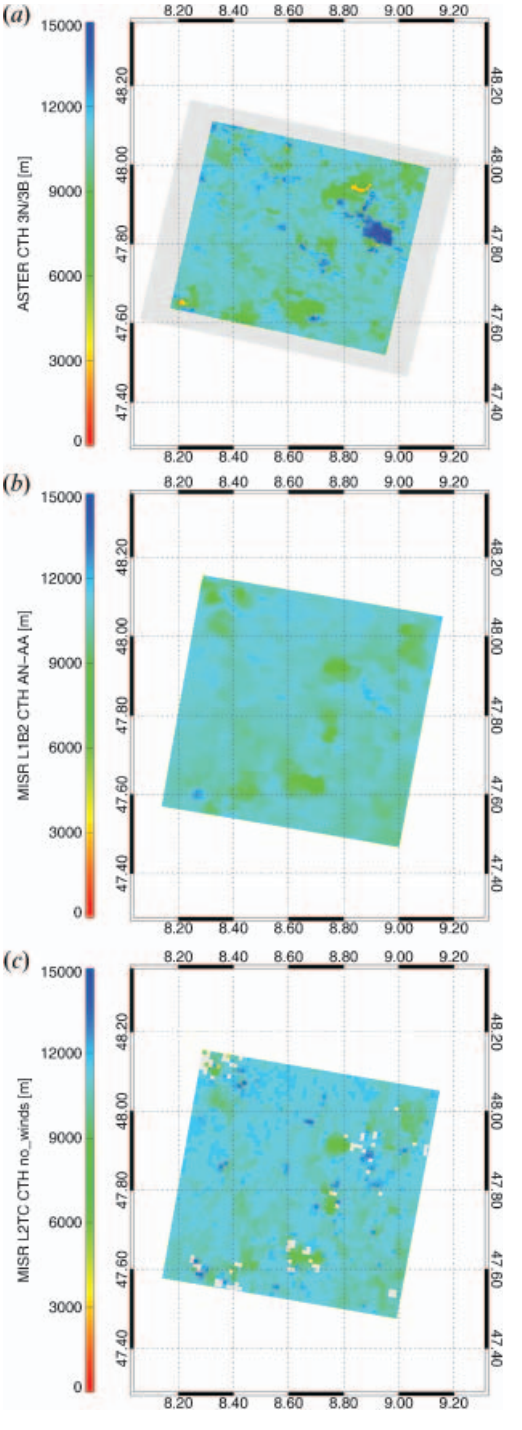


Figure 6. Cloud-top height (CTH) results from (*a*) ASTER (MPGC LSM), (*b*) MISR L1B2 An-Aa (MPGC LSM) and (*c*) MISR L2TC (M23) over Switzerland on 12 April 2002 (Terra orbit 12321). No cloud motion correction was applied to the data. The spatial resolution of the CTH grid is 15 m (ASTER), 275 m (MISR MPGC LSM) and 1100 m (MISR L2TC).

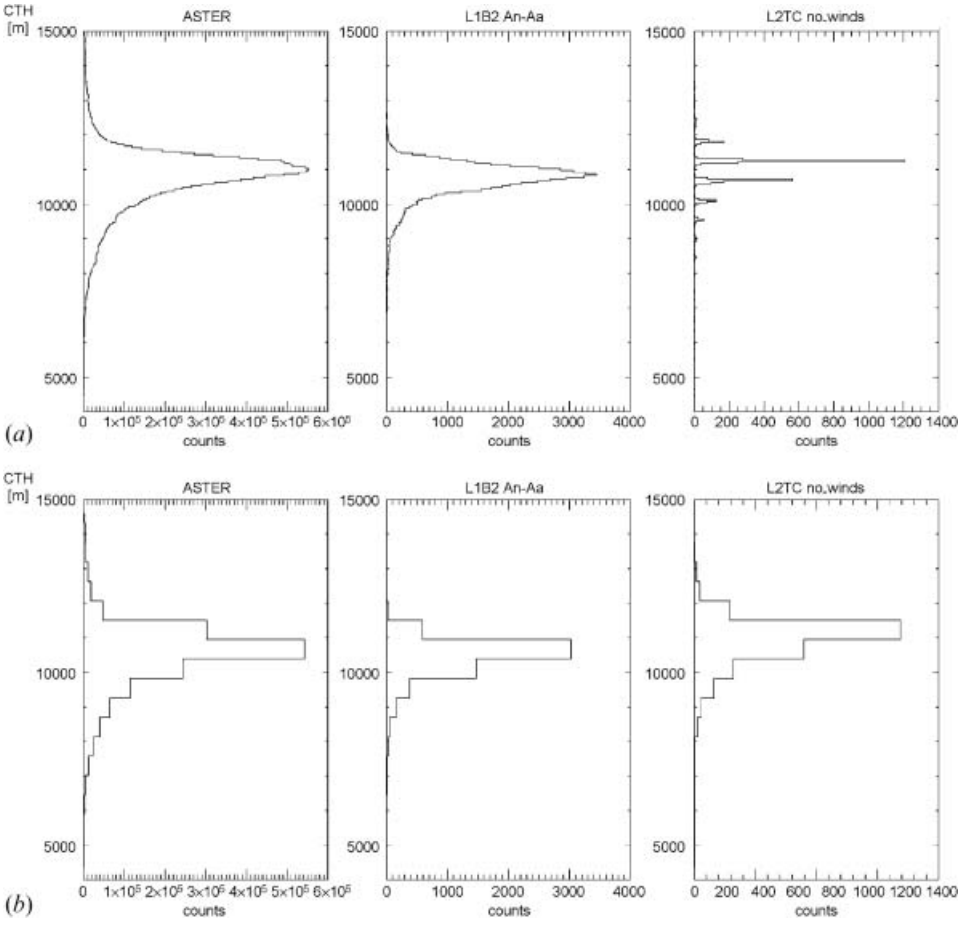


Figure 7. Cloud-top height (CTH) histogram for the results from ASTER (MPGC LSM) (left), MISR L1B2 An-Aa (MPGC LSM) (centre) and MISR L2TC (M23) (right) over Switzerland on 12 April 2002 (Terra orbit 12321). The spatial resolution of the CTH grid is 15 m (ASTER), 275 m (MISR MPGC LSM) and 1100 m (MISR L2TC). No cloud motion correction was applied to the data. (a) Histogram bin size=50 m, (b) histogram bin size=280 m.

to retrieve relative stereo CTHs (without cloud advection correction) with an accuracy of 12.5 m (ASTER) and 280 m (MISR), respectively, using a sub-pixel LSM algorithm with an accuracy within clouds of about $\pm 0.5$ pixels. For the case study considered here, the CTH distributions from both instruments agreed within these uncertainties, using 50 m height intervals. The MISR operational product, which does not implement a sub-pixel approach due to timing restrictions, has a higher uncertainty in CTH of about 560 m, but nonetheless produces a height distribution that is consistent with the more precise techniques when binned at 280 m intervals.

We note that the relative CTH from ASTER can also be readily corrected for the advection error, using cloud motion vector information from MISR triplets or from an external data source such as Meteosat-6 10-minute Rapid Scans. This would typically add a bias error to the absolute height retrieval of about 100 m for every

1 m/s uncertainty in the component of the cloud motion vector that is aligned with the direction of the Terra orbital track.

In practical terms, 3D high-resolution cloud analyses from ASTER cannot be applied to many scenes, as ASTER is only switched on during very short time intervals each day (on-demand) and mainly over non-cloudy land areas. Therefore, a systematic cloud geometry analysis from ASTER would be very difficult to schedule. However, it is expected that this ASTER/MISR synergy for clouds will be further exploited in specific measurement campaigns, by early scheduling of on-demand ASTER data acquisition.

**Acknowledgements**

The EOS-Terra MISR data (level 1B2 and level 2TC) were obtained from the NASA Langley Research Center Atmospheric Sciences Data Center and the ASTER data were received from the Japanese ASTER User Service. We thank Catherine Moroney and Ákos Horváth, Jet Propulsion Laboratory (JPL), for their assistance with understanding the L2TC products, and the ASTER project team for the on-demand data acquisition of ASTER over Zürich-Kloten, Switzerland. G. Seiz received funding from the Bundesamt für Bildung und Wissenschaft (BBW) within the EU-project CLOUDMAP2 (BBW Nr. 00.0355-1). Research by R. Davies was carried out at the JPL, under a contract with the National Aeronautics and Space Administration.

**References**

Abrams, M., 2000, The Advanced Spaceborne Thermal Emission and Reflection Radiometer (ASTER): data products for the high spatial resolution imager on NASA's Terra platform. *International Journal of Remote Sensing*, **21**, pp. 847–859.

Aster, 2002, ASTER Level1 Data Product. Technical report, ASTER science project. Available online at: www.gds.aster.ersdac.or.jp/gds_www2002/libraly_e/l1pdoc/AG-E-E-2209-R03-7-26.rtf.

Baltsavias, E.P., 1991, Multiphoto geometrically constrained matching. PhD dissertation, Institute of Geodesy and Photogrammetry, ETH Zurich, Mitteilungen No. 49.

Baltsavias, E. and Stallmann, D., 1993, SPOT stereo matching for DTM generation. *Proceedings of the Conference on Integrating Photogrammetric Techniques with Scene Analysis and Machine Vision*, 12–16 April, Orlando, USA. In *Proceedings of SPIE*, **1944**, pp. 152–163.

Diner, D., Davies, R., Di Girolamo, L., Horvath, A., Moroney, C., Muller, J.-P., Paradise, S., Wenkert, D. and Zong, J., 1999, MISR level 2 cloud detection and classification. JPL Technical report ATBD-MISR-07, Jet Propulsion Laboratory, California Institute of Technology, Pasadena, CA, USA. Available online at: http://eospso.gsfc.nasa.gov/eos_homepage/for_scientists/atbd/docs/MISR/atbd-misr-07.pdf.

Förstner, W. and Gülch, E., 1987, A fast operator for detection and precise location of distinct points, corners, and centers of circular features. In *Proceedings of the ISPRS Intercommission Conference on Fast Processing of Photogrammetric Data*, Interlaken, Switzerland, 2–4 June, pp. 281–305.

Fujita, T., 1982, Principle of stereoscopic height computations and their applications to stratospheric cirrus over severe thunderstorms. *Journal of the Meteorological Society of Japan*, **60**, pp. 355–368.

Grün, A., 1985, Adaptive least squares correlation: a powerful image matching technique. *South African Journal of Photogrammetry, Remote Sensing and Cartography*, **14**, pp. 175–187.

HARRIS, C. and STEPHENS, M., 1988, A combined corner and edge detector. In *Proceedings of the 4th Alvey Vision Conference*, Manchester, UK, 31 August–2 September, pp. 147–151.

HASLER, F., 1981, Stereographic observations from geosynchronous satellites: an important new tool for the atmospheric sciences. *Bulletin of the American Meteorological Society*, **62**, pp. 194–212.

HORVÁTH, Á. and DAVIES, R., 2001, Feasibility and error analysis of cloud motion wind extraction from near-simultaneous multiangle MISR measurements. *Journal of Atmospheric and Oceanic Technology*, **18**, pp. 591–608.

JOVANOVIC, V., LEWICKI, S., SMYTH, M., ZONG, J. and KORECHOFF, R., 1999a, MISR level 1 georectification and registration. JPL Technical report ATBD-MISR-03. Available online at: http://eospso.gsfc.nasa.gov/eos_homepage/for_scientists/atbd/docs/MISR/atbd-misr-03.pdf.

JOVANOVIC, V., SMYTH, M. and ZONG, J., 1999b, MISR level 1 in-flight geometric calibration. JPL Technical report ATBD-MISR-04. Available online at: http://eospso.gsfc.nasa.gov/eos_homepage/for_scientists/atbd/docs/MISR/atbd-misr-04.pdf.

JOVANOVIC, V., BULL, M., SMYTH, M. and ZONG, J., 2002, MISR in-flight camera geometric model calibration and georectification performance. *IEEE Transactions on Geoscience and Remote Sensing*, **40**, pp. 1512–1519.

LANG, H. and WELCH, R., 1999, *ASTER Digital Elevation Models (standard product AST14)*. Version 3.0. ATBD-AST-08, NASA JPL and University of Georgia.

LEWICKI, S., CHAFIN, B., CREAN, K., GLUCK, S., MILLER, K. and PARADISE, S., 1999, MISR data products specifications. Technical report, NASA JPL. Available online at: http://eosweb.larc.nasa.gov/PRODOCS/misr/readme/dps_ne_icd.pdf.

MORONEY, C., DAVIES, R. and MULLER, J.-P., 2002, Operational retrieval of cloud-top heights using MISR data. *IEEE Transactions on Geoscience and Remote Sensing*, **40**, pp. 1532–1540.

MULLER, J.-P., MANDANAYAKE, A., MORONEY, C., DAVIES, R., DINER, D.J. and PARADISE, S., 2002, MISR stereoscopic image matchers: techniques and results. *IEEE Transactions on Geoscience and Remote Sensing*, **40**, pp. 1547–1559.

PRATA, A. and TURNER, P., 1997, Cloud-top height determination using ATSR data. *Remote Sensing of Environment*, **59**, pp. 1–13.

SCHMID, C., MOHR, R. and BAUCKHAGE, C., 1998, Comparing and evaluating interest points. Available online at: ftp://ftp.inrialpes.fr/pub/movi/publications/schmid_iccv98_ext.ps.gz.

SEIZ, G., 2003, Ground- and satellite-based multi-view determination of 3D cloud geometry. PhD thesis, Institute of Geodesy and Photogrammetry, ETH Zürich, Switzerland, 2003. IGP Mitteilungen No. 80. Available online at: http://e-collection.ethbib.ethz.ch/cgi-bin/show.pl?type=diss&nr=15172.

SEIZ, G., BALTSAVIAS, E. and GRÜN, A., 2003, High-resolution cloud motion analysis with Meteosat-6 Rapid Scans, MISR and ASTER. *EUMETSAT Meteorological Satellite Conference*, Weimar, 28 September–3 October 2003, EUM P39, pp. 352–358.

SNYDER, J., 1987, Map projections – a working manual. Technical report, USGS Professional Paper 1395.

URAI, M., 2004, Sulfur dioxide flux estimation from volcanoes using Advanced Spaceborne Thermal Emission and Reflection Radiometer – a case study of Miyakejima volcano, Japan. *Journal of Volcanology and Geothermal Research*, **134**, pp. 1–13.

WALLIS, R., 1976, An approach to the space variant restoration and enhancement of images. In *Proceedings of the Symposium on Current Mathematical Problems in Image Science*, Naval Postgraduate School, Monterey CA, USA, November.

YAMAGUCHI, Y., KAHLE, A., TSU, H., KAWAKAMI, T. and PNIEL, M., 1998, Overview of Advanced Spaceborne Thermal Emission and Reflection Radiometer (ASTER). *IEEE Transactions on Geoscience and Remote Sensing*, **36**, pp. 1062–1071.

ZONG, J., DAVIES, R., MULLER, J.-P. and DINER, D., 2002, Photogrammetric retrieval of cloud advection and top height from the Multi-Angle Imaging SpectroRadiometer (MISR). *Photogrammetric Engineering and Remote Sensing*, **68**, pp. 821–829.